New insights into the cathodic dissolution of aluminium using electrochemical methods

Mai Tran Tron Long, Bernard Tribollet, Eliane M M Sutter

New insights into the cathodic dissolution of aluminium using electrochemical methods

T.T.M. Tran[*], B. Tribollet, E.M.M. Sutter

Sorbonne Universités, UPMC Univ Paris 06, CNRS, Laboratoire Interfaces et Systèmes Electrochimiques, 4 place Jussieu, F-75005, Paris, France

* Corresponding author

E-mail address: mai.tran_trong_long@upmc.fr

Abstract

The cathodic dissolution of aluminium in neutral medium was studied by electrochemical methods. It is shown that oxygen reduction at the surface of the metal is kinetically controlled and that the diffusion regime is never reached due to the poor conductivity of the oxide film and consequently a high potential drop across the layer. Nevertheless, at E < -1.4 V/MSE, the rate of hydroxyl production during oxygen reduction is high enough to raise the interfacial pH above 9, causing chemical dissolution of the oxide layer. The oxide film was characterized by electrochemical impedance spectroscopy in the potential range where it is stable and does not undergo chemical dissolution. The analysis based on the use of the power law model and a Cole-Cole graphical representation allows extraction of the oxide film thickness and provides the resistivity profile in the layer. In the potential range close to the open-circuit potential (-1.4 V < E < E_{corr}), for the oxide layer formed during 2 hours in 10^{-2} M Na_2SO_4 solution, a constant thickness between 8 and 9 nm was determined and the resistivity varied between 10^{11} Ω cm^{-1} at the oxide/metal interface and 10^5 Ω cm^{-1} at the electrolyte/oxide interface. At more negative potential, the thickness of the layer and the resistivity at the electrolyte/oxide interface drop significantly due to alkalinisation of the interface which induces chemical dissolution of the oxide.

1. Introduction

Aluminium corrosion in aqueous neutral solutions has been widely investigated in the anodic range where a passive oxide/hydroxide layer provides a passive behaviour to aluminium [1-6]. Many experiments have also been performed on aluminium alloys (for instance AA 2024-T3 alloy) in which galvanic corrosion occurs between an aluminium matrix acting as anode and copper rich intermetallic particles acting as cathodes [7-10]. As a consequence, generation of high pH zones at the surface of the particles promotes chemical dissolution of the Al matrix in the vicinity of the particles. When pure aluminium is polarized in the cathodic range at neutral pH, Al dissolution is usually observed and the rate of aluminium dissolution increases with increasing cathodic polarization [11]. The mechanism by which the cathodic dissolution of aluminium occurs is now well understood and involves alkalinisation of the oxide/solution or aluminium/solution interfaces during oxygen and water reduction leading to chemical dissolution of the oxide or the metal [12-15]. The overall current measured in the cathodic potential range is consequently often the sum of an aluminium oxidation rate and an oxygen and water reduction rate at a surface which changes as a function of the applied potential. This makes complex the quantitative use of data from the polarization curves for predicting the aluminium cathodic dissolution rate, requiring complementary methods to measure separately the anodic and cathodic contributions of the overall current and to distinguish the chemical from the electrochemical contributions. For instance, the quartz crystal microbalance technique has been used to determine the rate of Al dissolution, whereas measurements of H_2 evolution during water reduction was used to estimate the rate of the cathodic reaction [11].
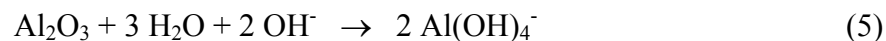
Ogle *et al* [16, 17] used atomic emission spectroelectrochemistry (AESEC) to follow the Al dissolution rate during the cathodic polarization of an aluminium electrode. They demonstrated that cathodically generated hydroxide is responsible for chemical dissolution of the oxide/hydroxide layer formed at the open-circuit potential. It is followed by oxidation of the aluminium substrate for rebuild the passive layer which is therefore present on the substrate at all applied potentials, up to 1 V negative to the open-circuit potential.

The following reactions have to be considered:

Electrochemical reactions:

$$2\,H_2O + 2\,e^- \;\rightarrow\; H_2 + 2\,OH^- \tag{1}$$

$$O_2 + 4\,e^- + 2\,H_2O \;\rightarrow\; 4\,OH^- \tag{2}$$

$$Al + 3\,OH^- \;\rightarrow\; Al(OH)_3 + 3\,e^- \tag{3}$$

Chemical reactions at the alkaline interface:

$$Al(OH)_3 + OH^- \;\rightarrow\; Al(OH)_4^- \tag{4}$$

$$Al_2O_3 + 3\,H_2O + 2\,OH^- \;\rightarrow\; 2\,Al(OH)_4^- \tag{5}$$

In reaction (3) only $Al(OH)_3$ is assumed for simplicity to be formed, though $AlOOH$ and Al_2O_3 are also expected to be present in the deposited layer [15]. Since the oxide/hydroxide layer at a given potential exists in a steady state between chemical film dissolution (reaction 4) and film reformation after aluminium anodic dissolution (reaction 3), it is likely to be modified with time and with applied potential. Consequently the rate of the cathodic reaction which occurs at the surface of the film is expected to depend on the properties of the film and cannot be determined using classical electrochemical approaches like potentiodynamic experiments. According to Serdechnova *et al* [15], the cathodic dissolution rate for aluminium is linearly proportional to the hydroxide generation rate (cathodic reaction) with a stoichiometry of OH^-/Al^{3+} of about 4.62.

The aim of the present work is to improve the electrochemical approach and to show that Electrochemical Impedance Spectroscopy (EIS) is able to provide further inside into the mechanism of cathodic dissolution of aluminium.

EIS has been shown to be a powerful method for separating different electrochemical contributions to the overall reaction and also to provide quantitative estimation of the properties of an oxide layer using numerical simulation [18-21]. This method is used in the present case at different cathodic potential values where oxygen reduction is assumed to be the main cathodic reaction (ORR).

2. Experimental

A pure aluminium electrode (99.95% weight purchased from Goodfellow®, containing 50 ppm Fe and 100 ppm Si) of 0.2 cm^2 surface area, and occasionally a pure copper electrode (99.9% weight) were used as working electrodes. They were mechanically polished with silicon carbide papers (up to 1200 grade), then ultrasonically cleaned with distilled water and dried with a N$_2$ flux were used as working electrodes. A saturated mercury sulphate electrode (MSE; +0.645 V/SHE) as the reference electrode and a large platinum grid used as the counter electrode were introduced with the working electrode in a classical three electrode electrochemical cell.

Electrolytes were prepared from analytical grade reagents (Prolabo® Normapur): anhydrous sodium sulphate (Na$_2$SO$_4$) and sodium hydroxide (NaOH) using deionised water. The measurements were performed in 10^{-2} M Na$_2$SO$_4$ solution at pH 6.1. If necessary the pH was adjusted by addition of a dilute NaOH solution and a buffer solution at pH 7 provided by Hach® was used for comparison. The pH at the vicinity of the electrode surface was measured with a flat pH electrode (Mettler-Toledo® InLab Surface). The measurements were

performed at room temperature in air saturated solutions or in oxygen free solutions obtained after nitrogen bubbling during 30 min.

All the electrochemical measurements were performed using an electrochemical interface (SI1286, Solatron) coupled with a frequency response analyser (SI1250, Solatron). For the EIS measurements the applied frequency domain ranged from 65 kHz to 10 mHz with 12 points per decade. The sinusoidal perturbation was 5 mV peak to zero. The recorded spectra were analysed as Nyquist and Bode diagrams. They were fitted using a home made simplex procedure. The program used minimises the χ^2 function defined below:

$$\chi^2 = \sum_{i=1}^{nf}\left[\left(\frac{Z_{re,i}-Z_{rc,i}}{|Z_e|}\right)^2 + \left(\frac{Z_{je,i}-Z_{jc,i}}{|Z_e|}\right)^2\right] \tag{6}$$

In this equation, nf, Z_r, Z_j and $|Z|$ represent, respectively, the total number of frequencies constituting the impedance spectra, the real and imaginary part and the modulus of the impedance. The subscripts e and c indicate variables relevant to experimental and calculated data respectively.

The surface of the working electrode was observed after different electrochemical treatments using a scanning electron microscope (Leica Stereoscan 440) equipped with EDX spectrometer. The XRD characterization was carried out by Panalytical Empyrean system using Cu K$_\alpha$ radiation ($\lambda = 1.54$ Å).

3. Results and discussion

3.1. Potentiodynamic cathodic curves

Polarization curves for aluminum obtained at a scanning rate of 1 mV s^{-1} are shown in Figure 1. Curves a (oxygen free) and b (air saturated) were drawn starting from the corrosion potential E_{corr} towards more cathodic values after immersion during 30 min in a 10^{-2} M Na$_2$SO$_4$ solution. Since in the oxygen free solution reduction of water is the only expected

reaction (curve a), the cathodic current observed in the air saturated solution in the potential range (-1.25 V to about -1.45 V) can be attributed to oxygen reduction (curve b). In the overall potential range reported in Figure 1, three distinct behaviours can be observed: in the potential range negative to -1.58 V curves a and b are superimposed and are therefore attributed to water reduction (domain III). In domain I ranging from E_{corr} to -1.40 V, a sharp current increase is followed by a short linear region. At -1.40 V, a clear modification of the shape of the curve is observed. The region between -1.40 and -1.58 V will be called domain II.

It is noticeable that when the curve starts from the cathodic range (-1.7 V) towards E_{corr} (curve c), it does not superimpose with curve b and the current density is even 2.5 times higher than for curve b between -1.25 and -1.40 V.

For comparison, the cathodic current at a bare copper surface obtained after cathodic polarization (curve d) in an air saturated solution shows a well defined current plateau due to diffusion limited oxygen reduction, which is the expected behaviour for ORR at a bare metallic surface. A rough calculation of the theoretical diffusion current density i_{diff} according to equation (7):

$$i_{diff} = \frac{n_{O_2} F D_{O_2} C_{O_2}}{\delta_N} \tag{7}$$

with $n_{O2} = 4$, Faraday constant $F = 96500$ C mol^{-1}, D_{O2} (oxygen diffusion coefficient) = 2 10^{-5} cm^2 s^{-1}, C_{O2} (oxygen concentration in the bulk) = 0.225 10^{-6} mol cm^{-3}, δ_N the thickness of the Nernst diffusion layer which in stagnant conditions is often taken as 0.05 cm, leads to a diffusion current density of about 35 μA cm^{-2} which is in good agreement with the experimental value of Figure 1, curve d.

In the case of aluminium, zone I can clearly be attributed to the ORR (equation (1)) on the unmodified passive aluminium oxide/hydroxide layer. In zone II, chemical dissolution of the

passive layer according to reactions (4) and (5), followed by aluminium anodic dissolution and hydroxide deposition (equation 3) are expected to occur simultaneously with oxygen reduction. In zone III, water is likely to be reduced on the modified hydroxide layer $Al(OH)_3$.

3.2. Influence of the rotation rate on the cathodic current density.

Chronoamperometric measurements (not shown) were performed at different potentials belonging to domain I and II at different rotation rates Ω of the electrode between 0 and 1000 rotations per minute (rpm), evidencing no influence of the mass transfer on the cathodic current density. We must admit that oxygen reduction at the surface of the electrode is here not controlled by the rate of mass transfer in the solution, but is under pure kinetic control. This could result from a high potential drop across the insulating oxide layer, allowing only a small part of the applied potential to affect the oxide/solution interface. It follows that the current density at the interface stays under kinetic control. This assumption is corroborated by Figure 1 showing that the cathodic current on aluminium never reaches the diffusion limited current plateau on copper in the whole cathodic domain under study. Unfortunately the very short linear branches in the experimental cathodic curves hinder the determination of hypothetical Tafel slopes b_c in the 10^{-2} M Na_2SO_4 solution.

3.3. Morphology of the surface of the electrode after cathodic polarization

Aluminium samples were polarized during 5 hours at -1.30 and -1.45 V in the 10^{-2} M Na_2SO_4 solution at $\Omega = 0$ rpm and the surface was observed using SEM (Figure 2 b and c) and analyzed by EDX. At the two potentials, Al and O are the main elements, in agreement with the conclusion of ref [14] that oxide (and/or hydroxide) is present in the whole potential range negative to the open-circuit potential. Additional analyses by XRD did not allow identifying more precisely the compounds in the layer because of their amorphous character.

A main difference between the two samples is that the surface seemed unchanged after polarization at -1.30 V, in comparison with the electrode before immersion (Figure 2 a), whereas holes and pits appeared in the layer after polarization at -1.45 V. In the latter case, Fe and Si were detected by EDX in some of the pits, suggesting the presence of intermetallic particles.

Several previous studies have clearly demonstrated that the corrosion of aluminium is influenced by the presence of low levels of iron, which is one of the main impurity elements present in commercial aluminium in the form of iron riche intermetallic particles [22-25]. The role of these particles is essential in the localized corrosion of aluminium alloys as the AA1xxx and AA6xxx series. At the corrosion potential, the cathodic reaction is assumed to occur on intermetallic phase and the anodic reaction is the passive current on the oxidized aluminium. The main effect is dissolution of aluminium and aluminium oxide around the intermetallic particles with the apparition of pits when particles have detached. The reactivity of the intermetallics has been shown to be particularly important in the presence of chloride ions, and less important in a sulphate medium [24]. At the surface of the alloy used in the present work (99.95 % Al, 50 ppm Fe, 100 ppm Si) the amount of iron-rich intermetallics appears to be too low to induce pitting after 5 hours in the vicinity of the open-circuit potential (Figure 2b). Moreover according to [22], the cathodic reaction rate at the surface of the intermetallics is lowered in presence of Si. At -1.45 V/MSE, the effect of the Fe-rich intermetallics appears under the aspect of pits (Figure 2 c). For more cathodic potential, the overall dissolution is likely to be too important to evidence pits and the surface is covered with a gelatinous deposit (Figure 2 e) characteristic of aluminium hydroxide.

3.4. Interfacial pH measurements

Interfacial pH values during oxygen reduction in a neutral solution have been shown to reach alkaline values up to 10.7 on the diffusion plateau [26]. Since aluminium oxides and hydroxide are very soluble at alkaline pH [6], a pH electrode with flat bottom was used in the vicinity of the surface (at about 1 mm from the surface), to follow pH variation as a function of applied potential. The results are reported in Figure 3. It appears that in the potential range corresponding to domain I (between E_{corr} and about -1.40 V) the pH value rises up to 8.5. Then between -1.40 and -1.58 V (domain II), it reaches values close to 10. The pH measurements do not represent the interfacial pH values with accuracy, since the pH electrode is situated at 1 mm from the surface leading to underestimated interfacial values. Nevertheless they are consistent with the known reactivity of aluminium as a function of pH [6] showing a good stability between pH 4 and 9 but high solubility at higher pH.

A rough estimation of the interfacial pH at the limit between domains I and II can be provided taking the value of the stationary cathodic current at -1.40 V which is equal to 1 μA cm^{-2}, and taking the relation and numeric values from ref [26]:

$$N_{OH^-} = \frac{D_{OH^-}(C_{OH^-}(0) - C_{OH^-}(\infty))}{\delta_N} \tag{8}$$

N_{OH-} is the flux of hydroxide ions, D_{OH-} is the diffusion coefficient 2.57 10^{-5} cm^2 s^{-1} and a value of 0.05 cm for δ_N is taken as in equation (7). $C_{OH-}(0)$ and $C_{OH-}(\infty)$ are respectively the hydroxyl concentrations at the surface of the electrode and in the bulk of the solution. The solution pH being equal to 6, $C_{OH-}(\infty)$ can be neglected. From equation (8) an interfacial pH of 9.3 can be estimated, which is somehow higher than the experimental pH, as expected.

Interfacial pH measurements confirm that in domain I, oxygen reduction happens at the surface of a stable, insoluble but poorly conductive oxide/hydroxide layer, whereas in domain II it occurs at a surface which changes as a function of the applied potential due to the

solubility of the surface layer. This is in agreement with the SEM observations showing a non-damaged surface at -1.30 V (Figure 2 b) with no influence of intermetallics, and an attacked surface at -1.45 V (Figure 2 c) due to localized dissolution of aluminium around the intermetallics.

In order to check the influence of the interfacial pH on the cathodic current, potentiodynamic experiments were performed at different pH values of the solutions, between 6 and 11. A buffer solution at pH 7 was also used in order to keep the interfacial pH constant.

Figure 4 compares the behaviour of aluminium in the different solutions: for clarity only 3 curves are reported at pH 6.1, 11 and in the buffered solution at pH 7. Un-buffered solutions of pH 6.1 to 9 provide superimposed curves (not shown). At more alkaline pH (pH 11), the E_{corr} value is clearly shifted towards more negative potentials. For instance for curve a, an E_{corr} value as negative as -1.65 V is observed, generating an anodic current over a wide potential range negative to the open-circuit potential measured at neutral pH. This is in agreement with other works [15] showing that alkalinisation at the interface between Al and aqueous solution leads to oxide chemical dissolution enabling anodic dissolution of the Al substrate.

The potentiodynamic cathodic curve obtained in the buffered solution at pH 7, after 30 minutes of immersion in 10^{-2} M Na_2SO_4 solution, is superimposed with the curve at pH 6.1 between E_{corr} and about -1.4 V, but differs at more cathodic potentials. According to Figure 4, at E = -1.4 V, in un-buffered neutral solutions, the rate of ORR is sufficient to reach an interfacial pH close to 8.5 and consequently to enable chemical dissolution of the layer. The difference between the buffered and un-buffered curves at E < -1.4 V is mainly due to a modification of the oxide layer in the former case with partial chemical dissolution of the layer, anodic dissolution of the substrate followed by redeposition of a hydroxide layer from

the solution. In the buffered solution the layer is non-damaged as corroborated by the optical and SEM images of the surface (Figure 2 d and f).

Assuming that in the latter case the ORR occurs at a homogeneous aluminium oxide layer, the potentiodynamic cathodic curve obtained in the buffer solution was exploited to estimate the corresponding kinetic parameters. Figure 5 compares the cathodic curves on Al in the buffer solution to the cathodic curve at neutral pH on a copper electrode with same area. In the former case, 3 potential domains can be distinguished:

- In the -1.3 to -1.6 V, a Tafel behaviour is observed with a b_c value of 260 mV/log i.

- In the -1.6 to -1.9 V, a pseudo plateau appears.

- The potential domain negative to -1.9 V is assigned to water reduction. In comparison with the onset potential for water reduction at copper, an overpotential close to 400 mV can be observed.

In the Tafel domain: according to the definition of the Tafel coefficient b_c:

$b_c = 2.303RT/\alpha_c n_c F \approx 0.059/\alpha_c n_c$ and taking $n_c = n_{O2} = 4$ for the ORR

($R = 8.314$ J mol^{-1} K^{-1}, T = 298 K)

α_c is found to be close to 0.06.

This very low value is in agreement with a reaction rate occurring at a poorly conducting surface. It corresponds to a low charge transfer rate which stays the rate determining step of the overall reaction, explaining why the diffusion controlled regime for ORR can hardly be reached on aluminium.

In the -1.6 to -1.9 V potential range: potentiodynamic curves were obtained at different rotation rates ($\Omega = 0, 100, 500$ rpm) evidencing that the amplitude of the pseudo plateau was not influenced by the rotation rate of the electrode. As previously in the less cathodic domain, we must admit that the mass-transport-controlled regime on Al was not achieved.

The cathodic curve reported in linear coordinates (insert of Figure 5) shows a linear variation of the current density with potential in the -1.6 to -1.9 V potential range, similarly to an ohmic behaviour. An estimated value for the corresponding resistance is about $2 \ 10^4 \ \Omega \ cm^2$. We suggest that this represents the mean resistance of the layer R_{film}.

At -1.9 V: a current density of about $2 \ 10^{-5} \ A \ cm^{-2}$ is measured at the onset potential for water reduction. Taking $2 \ 10^4 \ \Omega \ cm^2$ for the film resistance leads to an estimate of 400 mV for the ohmic drop in the layer. This is in good agreement with the difference of overpotentials measured for water reduction between copper and aluminium (Figure 5) confirming our assumption.

In summary, the cathodic behaviour of Al in a buffer solution at pH 7 is controlled by the charge transfer resistance R_t at E > -1.6 V and by the film resistance at more cathodic potentials. Accordingly, the charge transfer resistance at E > -1.6 V is expected to be higher than $2 \ 10^4 \ \Omega \ cm^2$. When the potential decreases, R_t decreases, getting lower than $2 \ 10^4 \ \Omega \ cm^2$, and the overall behaviour is controlled by the ohmic drop in the layer.

A rough estimate with $R_{film} = 2 \ 10^4 \ \Omega \ cm^2$ for the film resistance, and 4 nm for the film thickness [27], provides a value of $5 \ 10^{10} \ \Omega \ cm$ for the film resistivity, which is a usual value for poorly conducting films.

3.5. EIS measurements in the cathodic potential range

EIS was used to characterize the properties and the evolution of the properties of the oxide layer on aluminium under cathodic polarization, this analysis was limited to the domain I where the unmodified passive oxide layer is present.

At corrosion potential (E_{corr} = -1.03 V/MSE)

The impedance diagrams at E_{corr} are reported in both Nyquist and Bode formats in Figure 6, after 2 hours of immersion at E_{corr} in the air saturated 10^{-2} M Na_2SO_4 solution. A single loop can be observed in the Nyquist plot showing poorly separated time constant. Two time constants are expected due to the oxide film and to the charge transfer respectively in the high and low frequency domain. At high frequency the depressed shape of the capacitive loop could be related to CPE behaviour for which the impedance is expressed as:

$$Z_{CPE} = \frac{1}{Q(j\omega)^{\alpha}}$$ (9)

where $\omega = 2\pi f$, Q has units of Ω^{-1} cm^{-2} s^{α} (or $F/s^{1-\alpha}cm^2$) and α is the CPE exponent [28]. To verify this assumption, the Bode diagrams, phase angle φ and modulus $|Z|$, were corrected for the ohmic resistance (electrolyte resistance R_e = 72 Ω cm^{-2}) and were also reported in Figure 6 [29]. In the modified Bode representation, the phase angle clearly shows a constant value of 71° between 200 Hz and 6.5 Hz, corresponding to CPE behaviour in this frequency range. Simultaneously the corrected modulus shows a linear domain in the log-log plot with a value of the slope equal to -α. In the present case a α value of 0.79 was graphically determined and corresponds to 71°/90° [28].

In the high frequency range (f > 200 Hz), the phase is no more constant. It first decreases by a few degrees than increases again (Figure 6 b). This behaviour is due to the geometry–induced current and potential distribution, as described in ref [30-31] for a disk electrode. The characteristic frequency f_c corresponding to the geometric effect is equal to $1/8R_eC$ [28], where C is the interfacial capacitance.

In the frequency domain in which a CPE behaviour was observed, Q values was calculated from the imaginary part of the impedance Z_j and from the α value [28] according to equation (10):

$$Q = \frac{1}{Z_j(f)(2\pi f)^{\alpha}} \sin\left(\frac{\alpha\pi}{2}\right)$$ (10)

In the present work, a mean Q value of $2.52 \ 10^{-5} \ \Omega^{-1} \ cm^{-2} \ s^{0.77}$ was estimated, in good agreement with the values provided by Jorcin *et al* [18] ($\alpha = 0.77$ and $Q = 1.7 \ 10^{-5} \ \Omega^{-1} \ cm^{-2} \ s^{0.77}$) for an oxide layer obtained on aluminium after 24 h immersion in air-saturated 0.1 M Na_2SO_4 solution.

Recently it has been shown that the film capacitance can be obtained from the extrapolation of the complex capacitance at infinite frequency using the usual Cole-Cole representation [32] (real and imaginary parts of the complex capacitance, C_r and C_j, as a function of frequency). Figure 7 a shows the capacitance plot obtained with the EIS data presented in Figure 6. The part of the curve corresponding to the CPE behaviour (f < 200 Hz) is a straight line crossing the origin in agreement with the theory presented in [32]. As expected, the curve deviates from linearity when the geometrical effect appears, in the high frequency range. In Figure 7 a at infinite frequency a value of 1.1 $\mu F \ cm^{-2}$ can be determined on the real axis for the interfacial capacitance C_{HF} which corresponds to the capacitance of the oxide C_{ox} in series with the double layer capacitance C_{dl}. At first approximation, since C_{dl} is usually at least one order of magnitude higher than C_{ox}, the interfacial capacitance C_{HF} can be taken equal to C_{ox}. Accordingly, the thickness of the oxide layer δ_{film} was deduced from equation (11):

$$\delta_{film} = \varepsilon\varepsilon_0/C_{ox} = \varepsilon\varepsilon_0/C_{HF} \qquad (11)$$

where ε_0 is the permittivity of vacuum ($\varepsilon_0 = 8.8542 \ 10^{-14} \ F \ cm^{-1}$), and ε is the dielectric constant of the layer which varies between 7.5 and 15 [19]. A value of 11.5 is chosen for ε in the present work leading to a value of 9.3 nm for the film thickness.

From the interfacial capacitance value and the electrolyte resistance value, the characteristic frequency f_c above which a geometry effect is expected is 1.6 kHz and is reported in Figure 6 b.

EIS in the cathodic potential range

The EIS was measured in the cathodic range between E_{corr} and -1.45 V. For each potential, the data were represented in a Cole-Cole plot, the value of the capacitance at infinite frequency assimilated to C_{ox} was determined, and the thickness of the oxide layer was deduced using equation 11. The results are plotted in Figure 8. For comparison the cathodic polarization curve is also represented on the same figure. It appears that the film thickness is roughly constant between E_{corr} and -1.3 V. At more cathodic potentials the thickness decreases and drops dramatically at about -1.45 V, when alkaline interfacial pH leads to chemical dissolution of the film, in agreement with the steady state measurements.

For comparison Cole-Cole plots obtained in the buffer solution are also reported in Figure 7 b, providing C_{HF} values very close to those obtained in Na_2SO_4 in the potential range positive to -1.45 V.

A CPE behaviour is generally attributed to a distribution of time constants either along the area of the electrode (surface distribution) or along the axis normal to the electrode surface (normal distribution) [18]. In the case of oxide films, the CPE behaviour is usually attributed to a normal time constant distribution induced by a significant variation of resistivity inside the films and the power-law model must then be used to analyse the impedance data [15]. The power-law model assumes the following distribution of resistivity:

$$\frac{\rho}{\rho_\delta} = \left(\frac{\rho_\delta}{\rho_0} + \left(1 - \frac{\rho_\delta}{\rho_0} \right) \xi^\gamma \right)^{-1} \tag{12}$$

where ξ is the dimensionless position in the film $\xi = x/\delta_{film}$, ρ_0 and ρ_δ are the boundary values of resistivity at the metal/oxide interface (x = 0, $\xi = 0$) and at the oxide/electrolyte interface (x $= \delta_{film}$, $\xi = 1$), respectively.

γ is a constant indicating how sharply the resistivity varies. Under the assumption that the dielectric constant is uniform, it was shown that

$$\gamma = \frac{1}{1-\alpha} \tag{13}$$

For a frequency lower than $f = 1/2\pi\varepsilon\varepsilon_0\rho_\delta$, the impedance of the oxide film is given by:

$$Z_{film} = g(\alpha)\frac{\delta_{film}\rho_\delta^{1-\alpha}}{\left(\rho_0^{-1} + j\omega\varepsilon\varepsilon_0\right)^\alpha} \tag{14}$$

where g is a function of α ($g = 1+2.88(1-\alpha)^{2.375}$).

It has to be noted that from equation 14, only the product $\delta_{film}\rho_\delta^{1-\alpha}$ can be obtained by regression. The values of δ_{film} have therefore to be fixed and were taken from the previous Cole-Cole plots.

EIS model:

The data analysis was performed in a potential range close to E_{corr} where the oxide layer did not undergo chemical dissolution (-1.45 < E < E_{corr}). In these conditions, the overall current is the sum of the anodic current corresponding to the passive current and the cathodic current corresponding to the ORR at the oxide-electrolyte interface. As shown previously, the rate of ORR is under pure kinetic control and can thus be characterized by a charge transfer resistance R_t. The electrons are transferred to the metal through the electronic resistance of the oxide film R_{film}. The anodic branch is correlated with the impedance of the oxide film in series with the double layer capacitance represented by a CPE. The whole equivalent circuit representing the interface is reported in Figure 9.

It is noticeable that the current is transported in the anodic branch by vacancies and ions and in the cathodic branch by electrons. Of course only the sum R_t+R_{film} can be regressed from the data. This equivalent circuit is also valid in the anodic potential range, but only the anodic branch is then used.

The regression of the experimental data is performed in the frequency range below 200 Hz since at higher frequencies the data are influenced by the geometry effect. The results of the regression are given in Table 1. From the CPE parameters corresponding to the double layer, the distribution of time constant is assumed to be along the electrode surface and the double layer capacitance was calculated using Brug's formula [33]:

$$C_{dl} = Q_{dl}^{1/\alpha} R_e^{(1-\alpha)/\alpha} \tag{15}$$

The corresponding values for C_{dl} are reported in Table 1. These values are in the usual range of double layer capacitance.

From the values of δ_{film} and from the boundary values of resistivity ρ_0 and ρ_δ, the distribution of resistivity in the oxide layer according to the power-law model (equation 12) could be obtained. In Figure 10 a distribution of resistivity is given throughout the thickness of the layer at two cathodic potentials: E = -1.15 V and E = -1.40 V. It is in agreement with the high resistivity of aluminium oxide.

As an example the comparison between the experimental data and the simulated impedance obtained from the fitted values given in Table 1 is given in Figure 10 b and c for two potentials in electrolyte-resistance-corrected Bode plots. The agreement is good in the whole frequency range; the small difference appearing in the high frequency range is attributed to current and potentials distribution induced by geometry effect, which were not taking into account in the model. It has to be noted that the presence of Fe-rich intermetallic phases can also contribute to the nonuniformity of the surface [22-25], but their influence were considered to be negligible in comparison with that of the classical nonuniform current distribution on the disk electrode in the present work.

A more accurate value for C_{ox} can be obtained from C_{HF} and C_{dl} values according to equation (16):

$$\frac{1}{C_{HF}} = \frac{1}{C_{ox}} + \frac{1}{C_{dl}} \tag{16}$$

The comparison shows that neglecting the double layer capacitance and assimilating C_{ox} and C_{HF} result in an error between 5 and 10% in the oxide film thickness.

4. Conclusion

Cathodic dissolution of aluminium was investigated using electrochemical methods. Polarization curves performed in 10^{-2} M Na_2SO_4 solution showed that the diffusion controlled regime for ORR is never reached on aluminium surface. This is due to the poor conductivity of the oxide layer and to the high potential drop across the layer. The pH measurements during cathodic polarization showed that for E < -1.4 V, the interfacial pH reaches sufficiently high values involving the chemical dissolution of the oxide layer.

Electrochemical impedance spectroscopy was used to characterize the oxide in the potential range where it is stable and does not undergo chemical dissolution. The analysis was based on the use of the power law model and a Cole-Cole graphical representation. These two approaches allow extraction of the thickness of the oxide layer and provide the resistivity profile in the layer. In the potential range close to the open-circuit potential (E_{corr} -300 mV < E < E_{corr}), a constant thickness between 8 and 9 nm was determined and the resistivity varied between 10^{11} Ω cm^{-1} at the oxide/metal interface and 10^{5} Ω cm^{-1} at the electrolyte/oxide interface. At more negative potential, the thickness of the layer drops significantly due to alkalinisation of the interface which induces chemical dissolution of the oxide.

References

[1] K. Hebert, R. Alkire, Dissolved metal species mechanism for initiation of crevice corrosion of aluminium, J. Electrochem. Soc. 130 (1983) 1001.

[2] O. Guseva, P. Schmutz, T. Suter, O. von Trzebiatowski, Modelling of anodic dissolution of pure aluminium in sodium chloride, Electrochim. Acta 54 (2009) 4514.

[3] M. Verhoff, R. Alkire, Experimental and modelling studies of single pits on pure aluminum in pH 11 NaCl solutions, J. Electrochem. Soc. 147 (2000) 1349.

[4] F.J. Martin, G.T. Cheek , W.E. O'Grady, P.M. Natishan, Impedance studies of the passive film on aluminium, Corros. Sci. 47 (2005) 3187.

[5] Z. Szklarska-Smialowska, Pitting corrosion of aluminium, Corros. Sci. 41 (1999) 1743.

[6] M. Pourbaix, Atlas des équilibres électrochimiques, Gauthier-Villars et Cie Ed., Paris, 1963.

[7] N. Birbilis, R.G. Buchheit, Electrochemical characteristics of intermetallic phases in aluminum alloys, J. Electrochem. Soc. 152 (2005) B140.

[8] T. Suter, R.C. Alkire, Microelectrochemical studies of pit initiation at single inclusions in Al 2024-T3, J. Electrochem. Soc. 148 (2001) B36.

[9] G.O Ilevare, O. Schneider, RG Kelly, J.R. Scully, In situ confocal laser scanning microscopy of AA-2024-T3 corrosion metrology, J. Electrochem. Soc. 151 (2004) B453.

[10] C. Blanc, N. Pébère, B. Tribollet , V. Vivier, Galvanic coupling between copper and aluminium in a thin-layer cell, Corros. Sci. 52 (2010) 991.

[11] Y. Baeck, G.S. Frankel, Electrochemical quartz crystal microbalance study of corrosion of phases in AA 2024, J. Electrochem. Soc. 150 (2003) B1.

[12] B.P. Caldwell, V.J. Alano, Rates of solution of zinc and aluminum while cathodic, Transactions of the Electrochemical Society 76 (1939) 271.

[13] K. Nisancioglu, H. Holtan, Cathodic polarization of commercially pure aluminium, Corros. Sci. 19 (1979) 537.

[14] S.M. Moon, S.I. Pyun, The corrosion of pure aluminium during cathodic polarization in aqueous solutions, Corros. Sci. 39 (1997) 399.

[15] M. Serdechnova, P. Volovitch, Fr. Brisset, K. Ogle, On the cathodic dissolution of Al and Al alloys, Electrochim. Acta 124 (2014) 9.

[16] M. Mokaddem, P. Volovitch, F. Rechou, R. Oltra, K. Ogle, The anodic and cathodic dissolution of Al and Al–Cu–Mg alloy, Electrochim. Acta 55 (2010) 3779.

[17] K. Ogle, M. Serdechnova, M. Mokaddem, P. Volovitch, The cathodic dissolution of Al, Al_2Cu, and Al alloys, Electrochim. Acta 56 (2011) 1711.

[18] J.-B. Jorcin, M. E. Orazem, N. Pébère, B. Tribollet, CPE analysis by local electrochemical impedance spectroscopy, Electrochim. Acta 51 (2006) 1473.

 [19] B. Hirschorn, M.E. Orazem, B. Tribollet, V. Vivier, I. Frateur, M. Musiani, Constant-phase-element behavior caused by resistivity distributions in films I. Theory, J. Electrochem. Soc. 157 (2010) C452.

[20] B. Hirschorn, M.E. Orazem, B. Tribollet, V. Vivier, I. Frateur, M. Musiani, Constant-phase-element behavior caused by resistivity distributions in films II. Applications, J. Electrochem. Soc. 157 (2010) C458.

[21] M. Musiani, M. E. Orazem, N. Pébère, B. Tribollet, V. Vivier, Constant-phase-element behavior caused by coupled resistivity and permittivity distributions in films, J. Electrochem. Soc. 158 (2011) C424.

[22] K. Nisancioglu, Electrochemical Behavior of Aluminum-Base Intermetallics Containing Iron, J. Electrochem. Soc. 137 (1990) 69.

[23] O. Seri, The effect of NaCl concentration on the corrosion behavior of aluminium containing iron, Corros. Sci. 36 (1994) 1789.

[24] J.O. Park, C.H. Paik, Y.H. Huang, R.C. Alkire, Influence of Fe-Rich Intermetallic Inclusions on Pit Initiation on Aluminum Alloys in Aerated NaCl, J. Electrochem. Soc. 146 (1999) 517.

[25] R. Ambat, A.J. Davenport, G.V.M. Scamans, A. Afseth, Effect of iron-containing intermetallic particles on the corrosion behaviour of aluminium, Corros. Sci. 48 (2006) 3455.

[26] C. Deslouis, I. Frateur, G. Maurin, B. Tribollet, Interfacial pH measurement during the reduction of dissolved oxygen in a submerged impinging jet cell, J. Appl. Electrochem. 27 (1997) 482.

[27] L.P.H. Jeurgens, W.G. Sloof, F.D. Tichelaar, C.G. Borsboom, E.J. Mittemeijer, Determination of thickness and composition of aluminium-oxide overlayers on aluminium substrates, Appl. Surf. Sci. 144–145 (1999) 11.

[28] M.E. Orazem, B. Tribollet, Electrochemical Impedance Spectroscopy, John Wiley & Sons, Hoboken, 2008.

[29] M. E. Orazem, N. Pébère, B. Tribollet, Enhanced graphical representation of electrochemical impedance data, J. Electrochem. Soc. 153 (2006) B129.

[30] V. M.-W. Huang, V. Vivier, M. E. Orazem, N. Pébère, B. Tribollet, The apparent constant-phase-element behavior of an ideally polarized blocking electrode: A global and local impedance analysis, J. Electrochem. Soc. 154 (2007) C81.

[31] V. M.-W. Huang, V. Vivier, I. Frateur, M. E. Orazem, B. Tribollet, The global and local impedance response of a blocking disk electrode with local constant-phase-element behaviour, J. Electrochem. Soc. 154 (2007) C89.

[32] M. Benoit, C. Bataillon, B. Gwinner, F. Miserque, M. E. Orazem, C. M. Sanchez-Sanchez, B. Tribollet, V. Vivier, Comparison of different methods for measuring the passive film thickness on metals, Electrochim. Acta 201 (2016) 340.

[33] G. J. Brug, A. L. G. Van Den Eeden, M. Sluyters-Rehbach, J. H. Sluyters, The analysis of electrode impedances complicated by the presence of a constant phase element, J. Electroanal. Chem. 176 (1984) 275.

Figure captions

Fig. 1. Cathodic polarization curves ($v = 1$ mV s^{-1}) on an aluminium electrode after 30 minutes of immersion in 10^{-2} M Na$_2$SO$_4$ solution:

a) deaerated - scanning direction $E_{corr} \rightarrow$ -1.7 V

b) aerated - scanning direction $E_{corr} \rightarrow$ -1.7 V

c) aerated - scanning direction -1.7 V $\rightarrow E_{corr}$

d) aerated - freshly polished copper surface - scanning direction -1.6 V $\rightarrow E_{corr}$

Fig. 2. SEM (a – d) and optical (e – f) images of an aluminium electrode:

(a) before immersion

(b) after 5 h at E = -1.30 V in aerated 10^{-2} M Na$_2$SO$_4$ solution

(c) after 5 h at E = -1.45 V in aerated 10^{-2} M Na$_2$SO$_4$ solution

(d) after 5 h at E = -1.87 V in aerated buffer solution at pH 7

(e) after cathodic sweep up to -1.7 V ($v = 0.01$ mV s^{-1}) in aerated 10^{-2} M Na$_2$SO$_4$ solution

(f) after cathodic sweep up to -1.9 V ($v = 0.01$ mV s^{-1}) in aerated buffer solution at pH 7.

Fig. 3. Comparison between polarization curve and interfacial pH values of an aluminium electrode in aerated 10^{-2} M Na$_2$SO$_4$ solution (immersion time: 30 minutes).

Fig. 4. Polarization curves ($v = 1$ mV s^{-1}) of an aluminium electrode after 30 minutes of immersion in aerated 10^{-2} M Na$_2$SO$_4$ solution at different pH:

a) 11.0

b) 6.1

c) buffer solution at pH 7

Fig. 5. Cathodic polarization curves ($v = 1$ mV s^{-1}) of:

a) Al - $\Omega = 100$ rpm - buffer solution at pH 7

b) Al - $\Omega = 500$ rpm - buffer solution at pH 7

c) Cu - $\Omega = 0$ rpm - 10^{-2} M Na$_2$SO$_4$ solution

Inset: enlargement of the domain between -1.6 and -1.8 V.

Fig. 6. Impedance diagram of an aluminium electrode in aerated 10^{-2} M Na$_2$SO$_4$ solution at E_{corr} (-1.03 V/MSE) after 2 h of immersion:

(a): Nyquist representation

(b): Bode representation $\log(|Z|)$ vs $\log(f)$ with (■) and without (○) electrolyte-resistance-correction

(c): Bode representation φ vs $\log(f)$ with (■) and without (○) electrolyte-resistance-correction

Fig. 7. Cole-Cole plots corresponding to EIS values of an aluminium electrode in aerated 10^{-2} M Na$_2$SO$_4$ or in buffer at pH 7 solutions (immersion time: 2 h in aerated 10^{-2} M Na$_2$SO$_4$)

(a): at E_{corr} (-1.03 V) in aerated 10^{-2} M Na$_2$SO$_4$ solution

(b): at different cathodic potentials in the two solutions

Fig. 8. Comparison between the cathodic polarization curve and the variation of the layer

thickness determined from Cole-Cole plots of an aluminium electrode in aerated

10^{-2} M Na_2SO_4 solution (immersion time: 2 h)

Fig. 9. Equivalent electrical circuit representing the Al/film/electrolyte interface

Fig. 10. Simulation of the behaviour of the Al/film/electrolyte interface at E = -1.15 and -1.40

V

(a): ρ vs δ

(b): Experimental and simulated impedance in electrolyte-resistance-corrected Bode

representation $\log(|Z|_{adj})$ vs $\log(f)$

(c): Experimental and simulated impedance in electrolyte-resistance-corrected Bode

representation φ_{adj} vs $\log(f)$

Figure 1

(a)

(e)

(f)
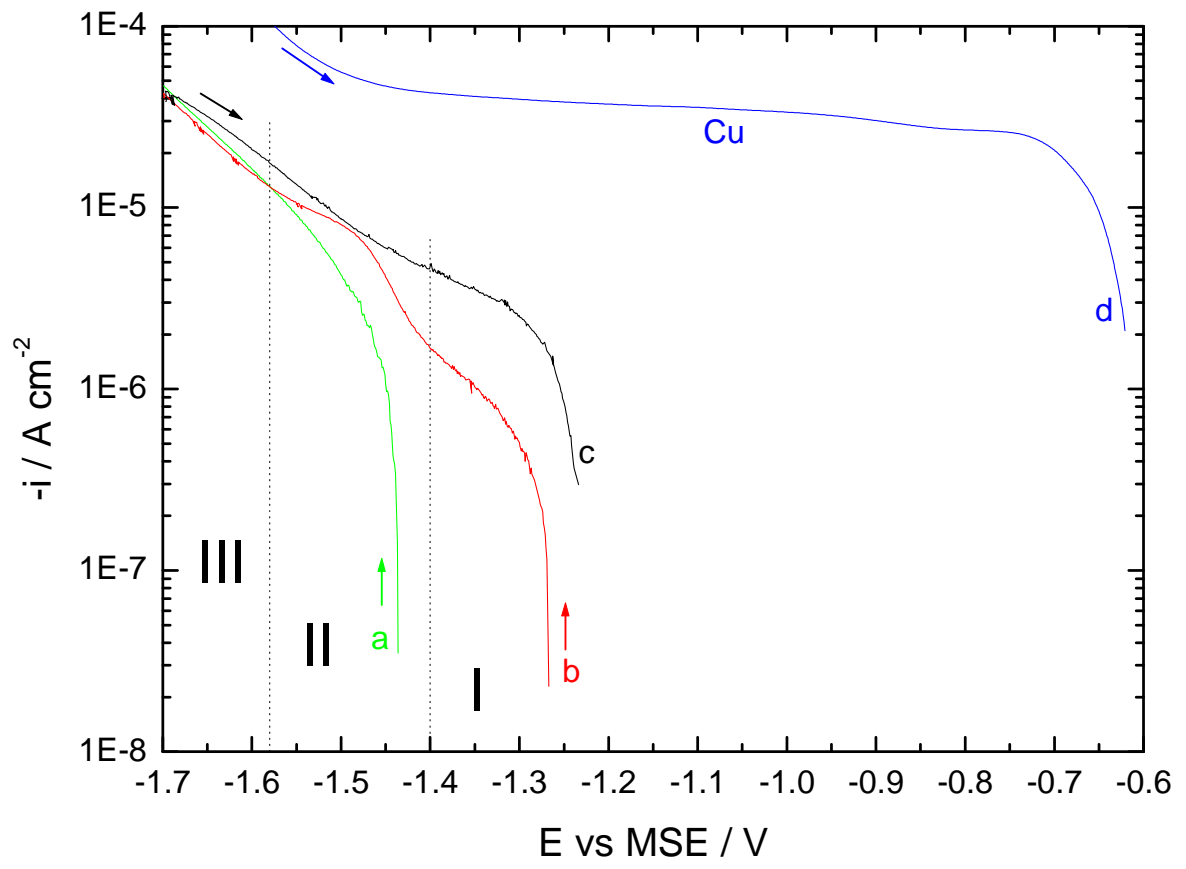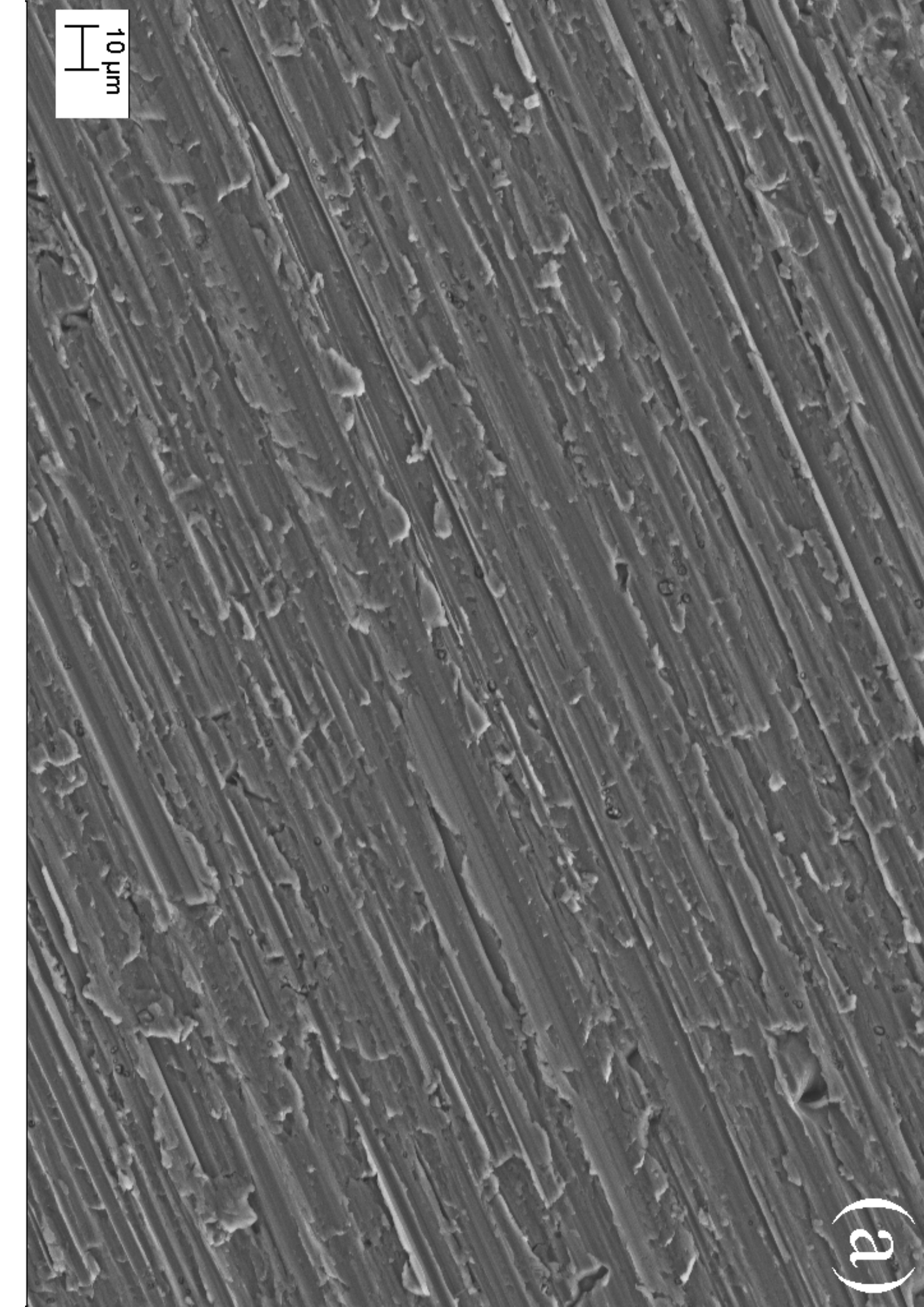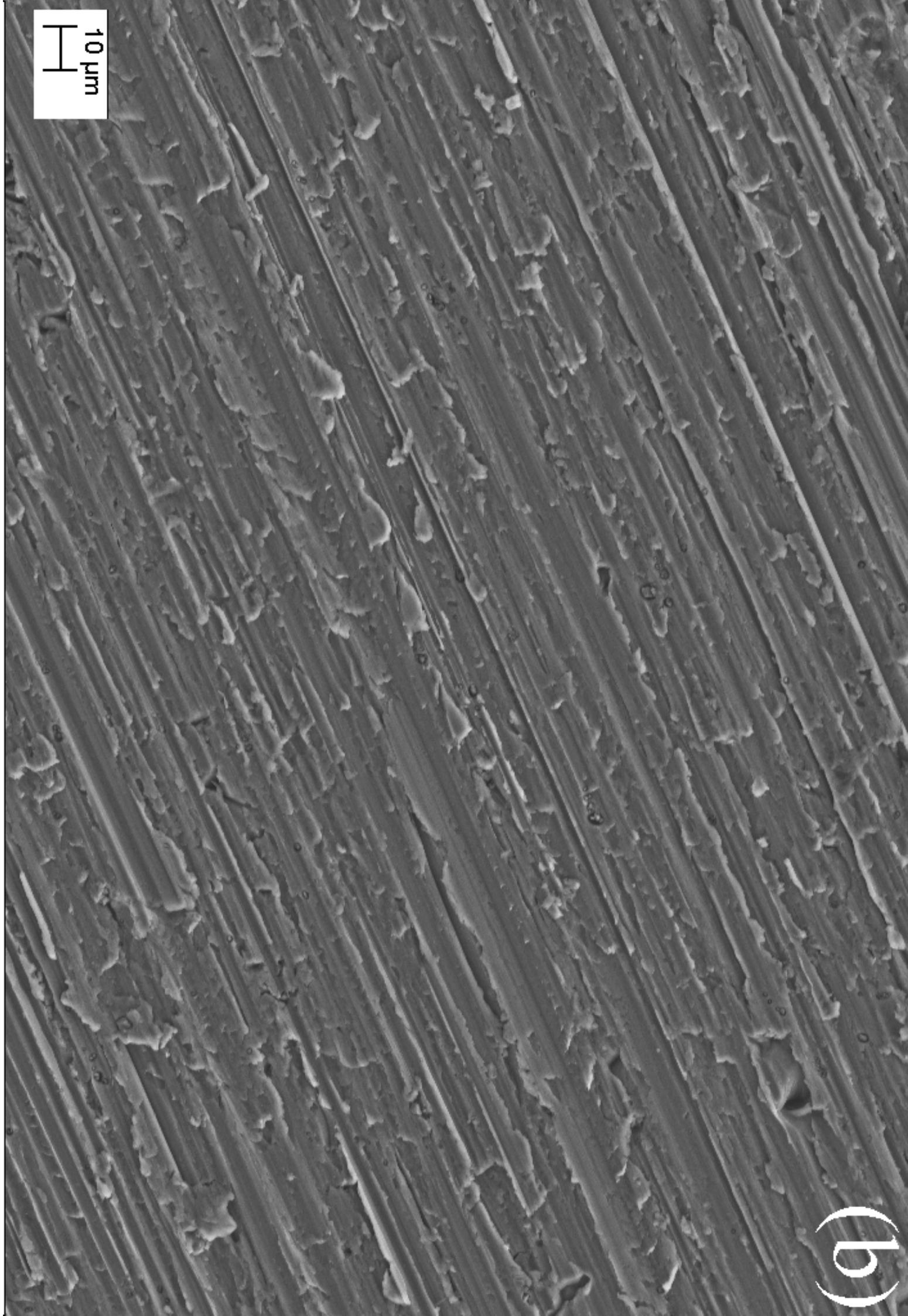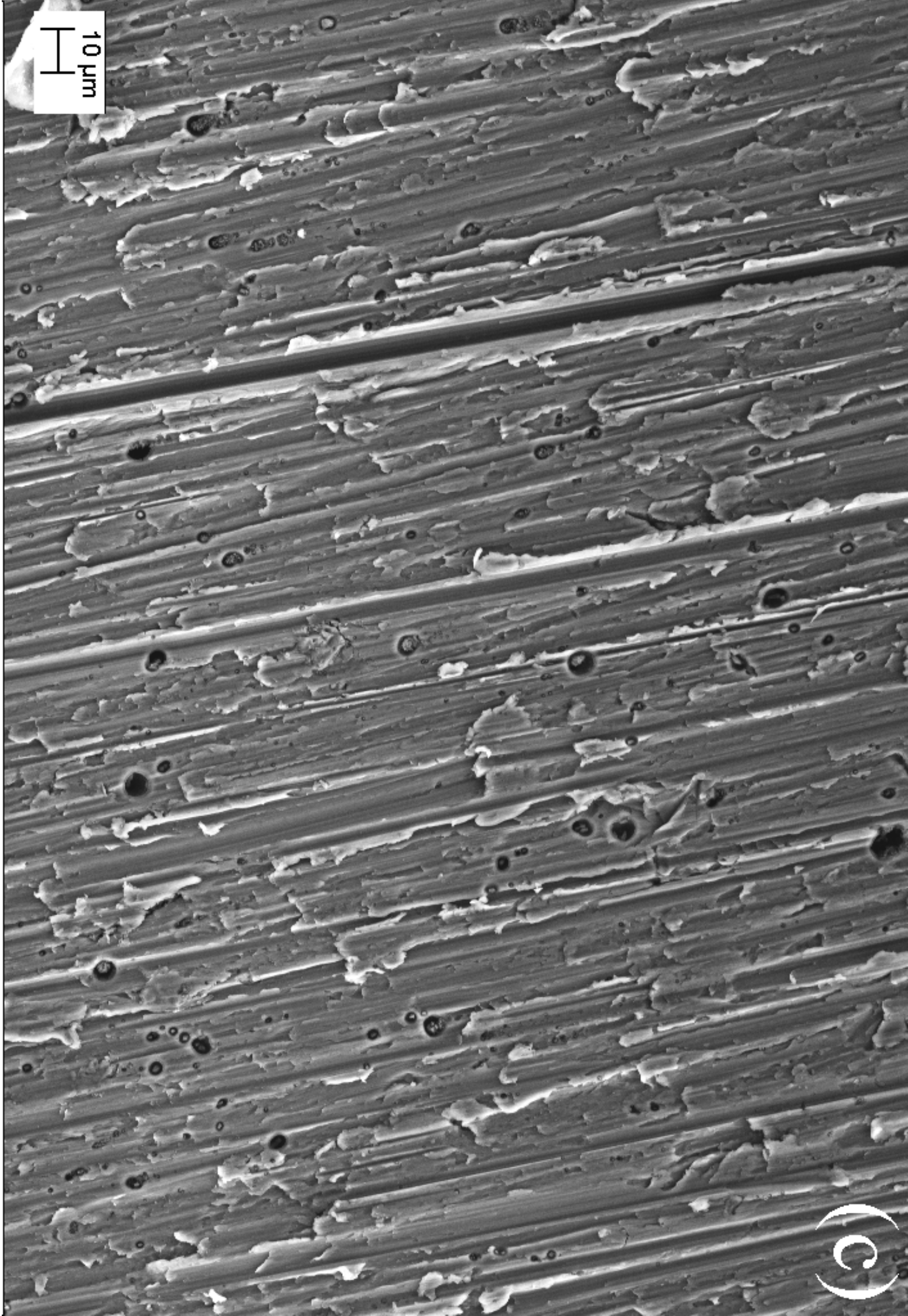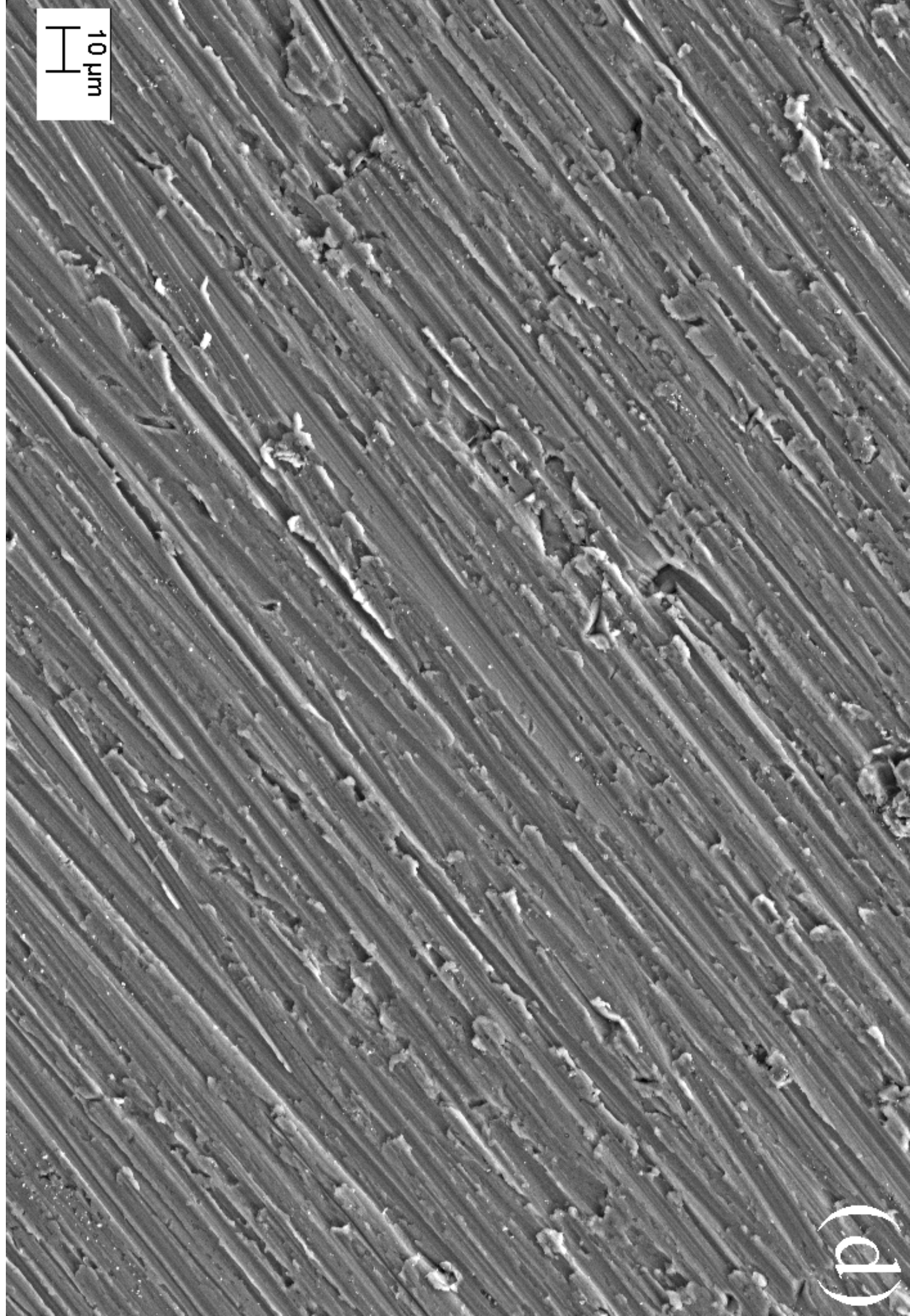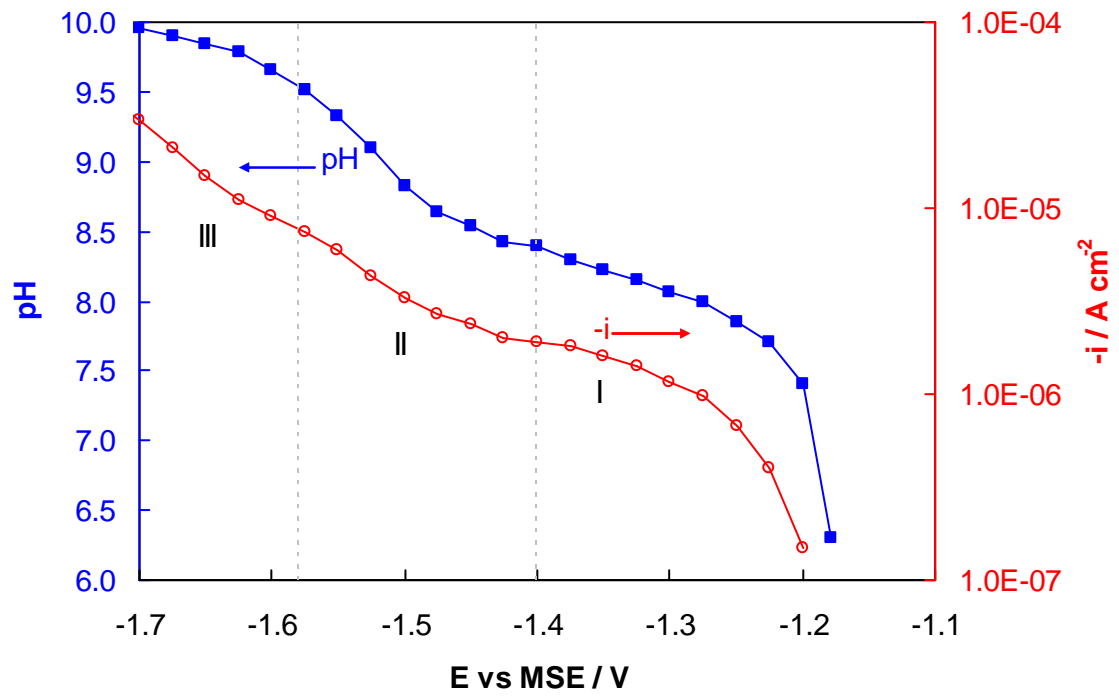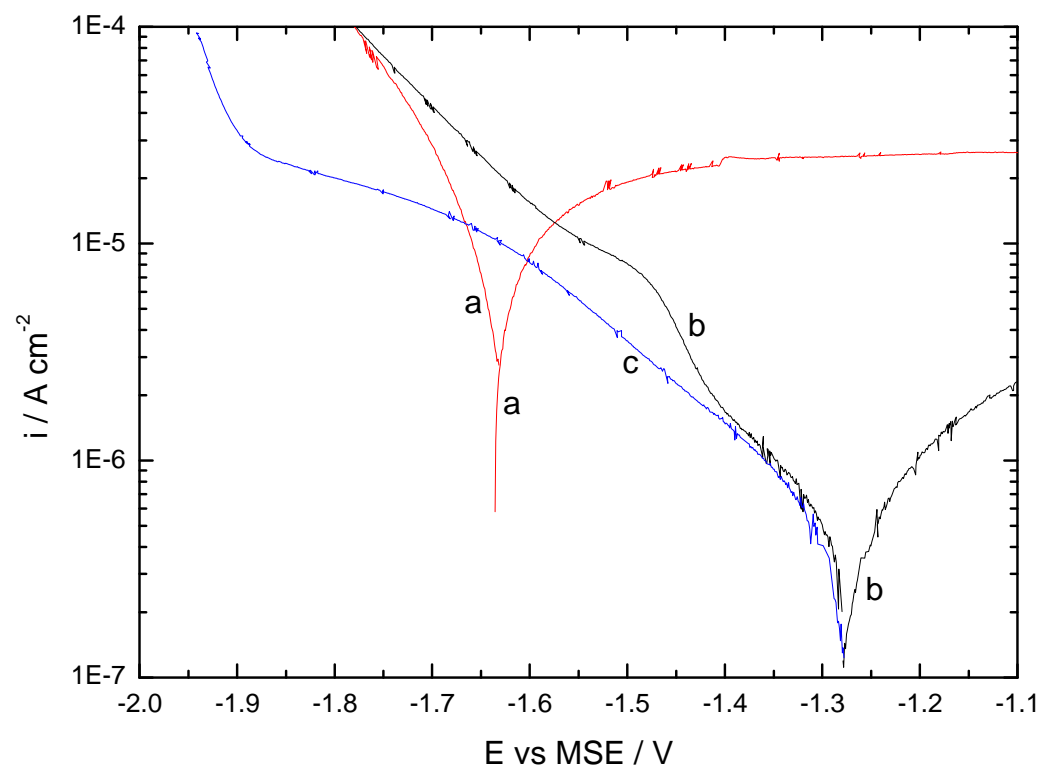
Figure 3

Figure 4

Figure 5
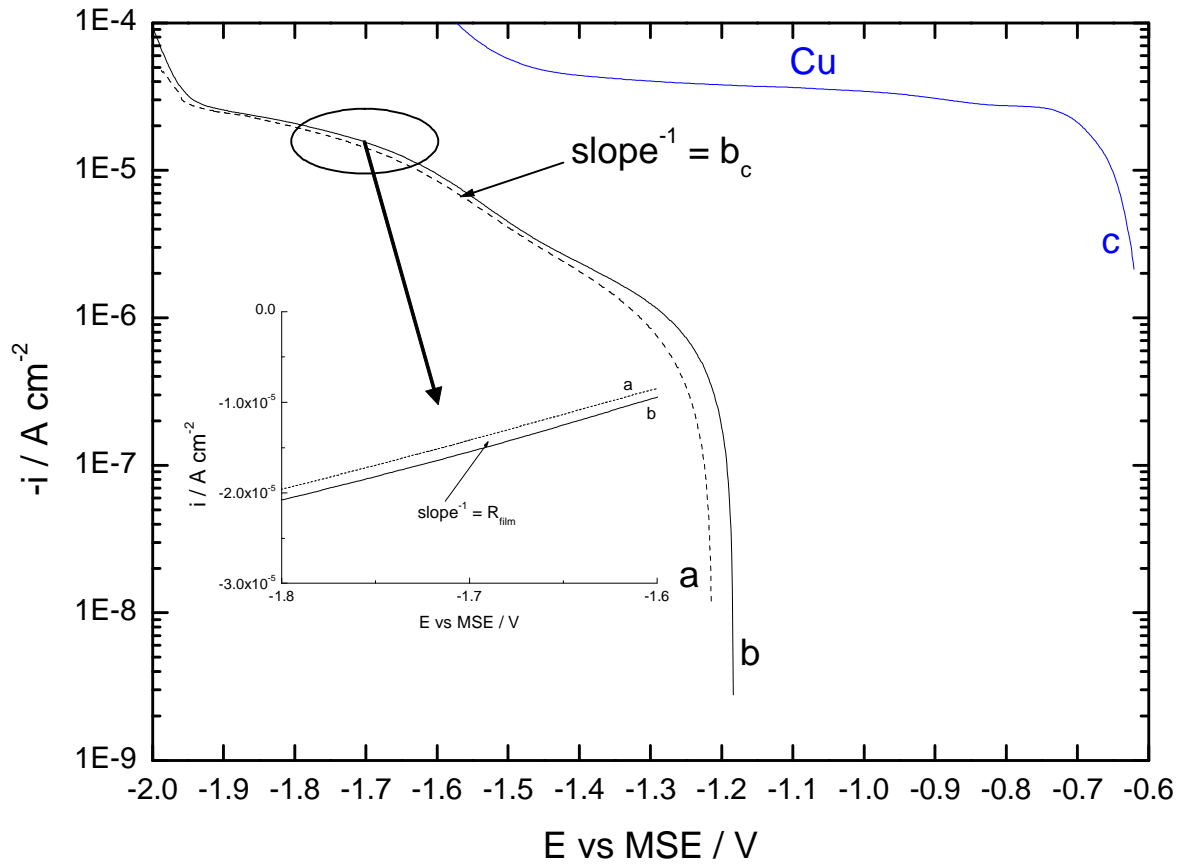
Figure 6
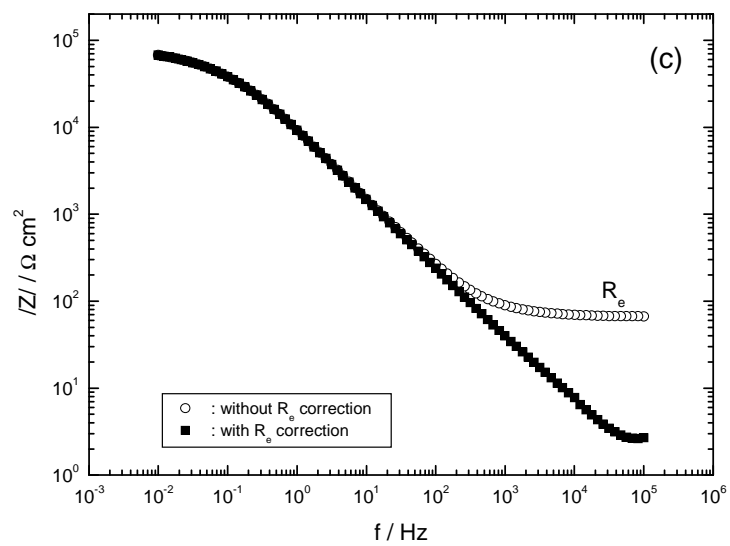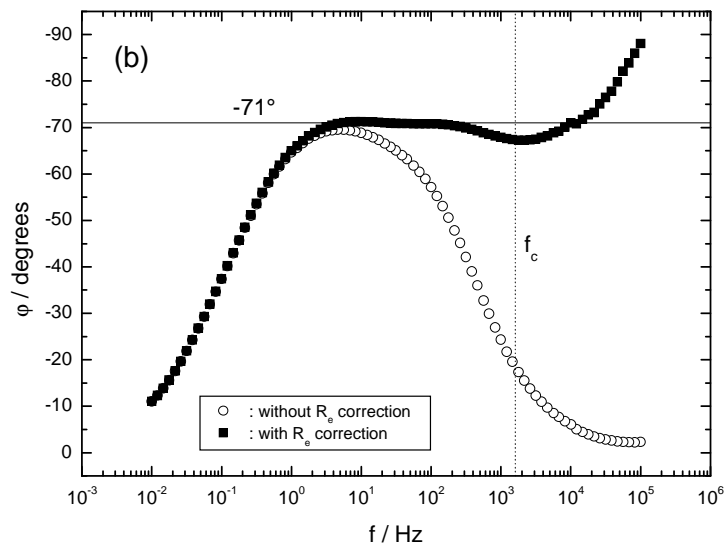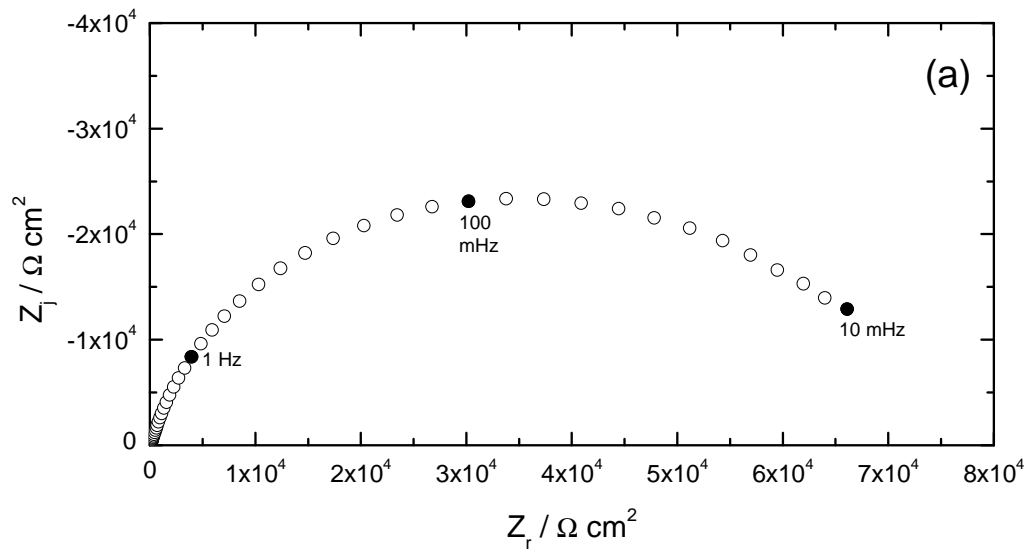
Figure 7
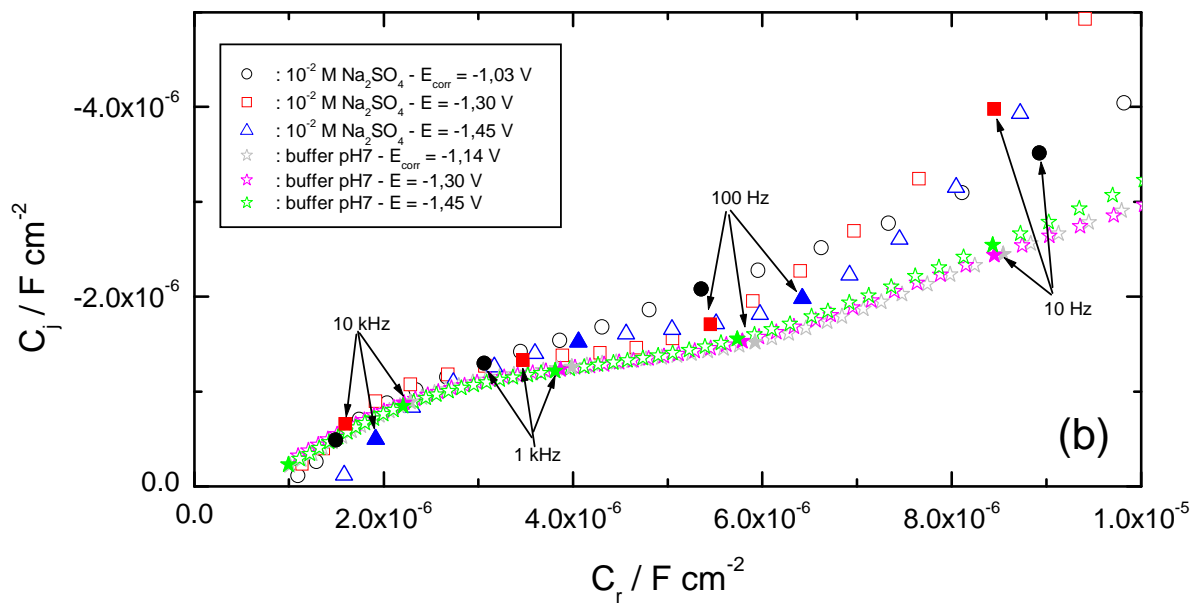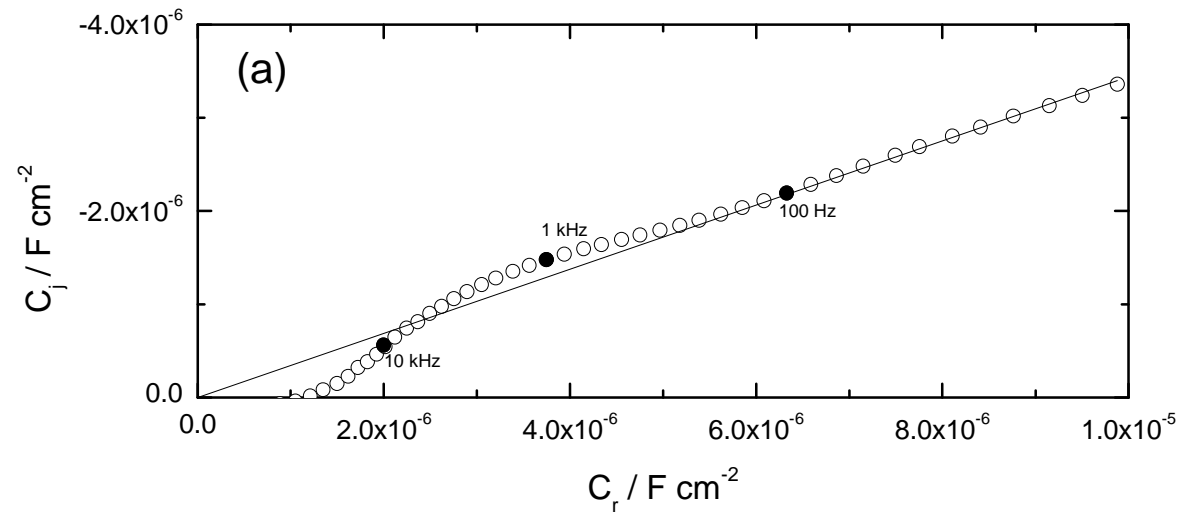
Figure 8

Figure 9

E $\mathrm{V/MSE}$	C_{HF} $\mu F\,cm^{-2}$	δ_{film} nm	α	ρ_0 $\Omega\,cm^{-1}$	ρ_δ $\Omega\,cm^{-1}$	Q_{dl} $Fs^{\alpha-1}cm^{-2}$	α_{dl}	C_{dl} $\mu F\,cm^{-2}$	$R = R_t + R_{film}$ $\Omega\,cm^2$
$E_{corr}=-1.03$	1.09	9.3	0.72	$4.8\ 10^{11}$	$8.5\ 10^5$	$3.97\ 10^{-5}$	0.90	20	$6.1\ 10^4$
-1.05	1.07	9.5	0.72	$4.0\ 10^{11}$	$7.4\ 10^5$	$3.89\ 10^{-5}$	0.88	18	$7.4\ 10^4$
-1.075	1.08	9.4	0.72	$3.5\ 10^{11}$	$1.1\ 10^6$	$4.05\ 10^{-5}$	0.92	24	$7.7\ 10^4$
-1.1	1.08	9.4	0.73	$3.1\ 10^{11}$	$1.1\ 10^6$	$4.35\ 10^{-5}$	0.93	29	$8.7\ 10^4$
-1.15	1.08	9.4	0.74	$2.2\ 10^{11}$	$6.9\ 10^5$	$4.54\ 10^{-5}$	0.86	18	$10.9\ 10^4$
-1.2	1.09	9.3	0.75	$1.4\ 10^{11}$	$1.7\ 10^5$	$4.87\ 10^{-5}$	0.81	13	$12.2\ 10^4$
-1.25	1.09	9.3	0.77	$1.3\ 10^{11}$	$8.2\ 10^4$	$5.22\ 10^{-5}$	0.80	13	$10.4\ 10^4$
-1.3	1.14	8.9	0.78	$1.2\ 10^{11}$	$6.5\ 10^4$	$5.23\ 10^{-5}$	0.80	13	$9.5\ 10^4$
-1.325	1.18	8.6	0.79	$1.1\ 10^{11}$	$6.5\ 10^4$	$5.31\ 10^{-5}$	0.81	14	$9.0\ 10^4$
-1.4	1.26	8.1	0.82	$0.8\ 10^{11}$	$5.4\ 10^3$	$5.74\ 10^{-5}$	0.76	10	$8.5\ 10^4$
-1.45	1.56	6.5	0.85	$0.5\ 10^{11}$	$9.1\ 10^2$	$5.94\ 10^{-5}$	0.77	11	$4.8\ 10^4$

Table 1. Parameters obtained from the regression of the experimental EIS data as a function of the cathodic potential.

Figure 10